



# Multiple vibrational resonance and antiresonance in a coupled anharmonic oscillator under monochromatic excitation

M PAUL ASIR, A JEEVAREKHA and P PHILOMINATHAN<sup>ID</sup>\*

Theoretical Research Laboratory, Department of Physics, AVVM Sri Pushpam College, Poondi, Thanjavur 613 503, India

\*Corresponding author. E-mail: philominathan@gmail.com

MS received 26 October 2018; revised 22 January 2019; accepted 26 February 2019; published online 21 June 2019

**Abstract.** We examine the existence of multiple vibrational resonance (VR) and antiresonance in two coupled overdamped anharmonic oscillators where each one is individually driven by a monochromatic sinusoidal signal with widely separated frequencies ( $\Omega \gg \omega$ ). In contemporary VR, superposed periodic waves are adopted to infer resonance, but herein we employ non-superposed periodic waves to acquire the elevated response. We study two coupling schemes namely, unidirectional and bidirectional, to substantiate the occurrence of multiple VR and antiresonance. Such occurrences have been shown and the results were ascertained with supportive numerical and experimental outcomes. We also illustrate the effect of coupling strength on the observed phenomenon.

**Keywords.** Coupled anharmonic oscillators; multiple vibrational resonance; antiresonance; mean residence time.

**PACS Nos** 05.45.–a; 05.90.+m

## 1. Introduction

Resonance, the maximum displacement in the magnitude spectrum of a system at particular frequencies, found a spotlight in the arena of physics, engineering and communication technologies. Among the several known resonance phenomena, stochastic resonance (SR) [1,2] attracted a great deal of attention among the research community as it exploits the productive role of noise in the amplification of a weak input signal. Recently, the ‘deterministic’ approach to describe and predict the SR phenomenon, based on replacing noise by high-frequency excitations, has been studied [3]. As noise is inexorable and ubiquitous, SR has drawn interdisciplinary attention from climate modelling [4] and signal processing [5] to neurophysiology [6–8]. After a brief interval, Landa and McClintock [9] reported a homologous phenomenon, namely vibrational resonance (VR) in a bistable system, where the amplification of a weak periodic component can be stimulated in the presence of an optimal high-frequency signal. Following the observation of VR in the bistable system, the study has been extended to monostable systems [10], excitable systems [11], time-delayed systems [12,13], maps [14] and so on, as structures employing widely varying frequencies find

extensive applications in communication and engineering. The development of atmospheric disturbance has also been described in terms of VR [15]. VR concerning the nonlinear response of the system was reported recently [16], where symmetry-breaking effect due to high-frequency component was manifested as the nonlinear response.

Further, non-autonomous coupled dynamical systems are pervasive in nature, and unravelling the physical phenomena associated with them becomes a non-trivial problem. Several intriguing observations, including synchronisation, amplitude death, chimera states and so on could be witnessed in such systems [17–19]. Among them, the resonant dynamics of coupled nonlinear systems has been a subject of extensive research in recent times due to its wide potential applications. To cite a few, stronger coupling strength in globally coupled Hodgkin–Huxley neurons can induce coherence resonance and synchronisation [20], theoretical and experimental verification of fano resonances in coupled plasmonic system [21], chemical synaptic coupling in three Fitzhugh–Nagumo neurons shows enhanced response under the influence of high-frequency driving [22], one-way coupled bistable system attributed to high- and low-frequency displays

improved signal transmission [23]. In particular, VR and SR have been ascertained in nonlinearly coupled overdamped anharmonic oscillators driven by amplitude-modulated periodic force and noise [24, 25]. In addition, multiple VR with extreme application facets in signal transmission and communication technologies have been reported in discrete systems [26], one-way coupled  $n$ -Duffing oscillator [27], quintic oscillator with monostable potential [28] and in a neuron model induced by dynamics of  $\text{Na}^+$  and  $\text{K}^+$  ions [29]. On the other hand, antiresonance leads to umpteen number of real practical applications including designs of chemotherapeutic protocols [30], robust dynamic model updating [31], desynchronising undesired oscillations [32], etc. have been reported. Specifically, Zhang *et al* [33] indicate the antiresonance behaviour as mode localisation in the frequency domain of weakly coupled micromechanical resonator sensors. As an added credit, antiresonance has been used for minimising undesired vibrations of certain parts of the system in aerospace and mechanical engineering.

A sweeping generalisation made out of the aforementioned studies is that either VR or SR is observed in nonlinear systems when excited by superposed biharmonic signals or a periodic signal combined with noise. But, a question can be raised whether VR can be induced in a coupled system, when both of them are driven by distinct and unique frequencies (figure 1). The present study aims at addressing the constraints such as (i) restriction on the modulation of additional periodic signals in coupled oscillating systems and (ii) denial of accessing the individual nodes or subsystems in a hybrid or complex network. Motivated by these aspects, we had set the following objectives:

- To investigate the VR and antiresonance phenomena in a unidirectionally coupled overdamped oscillator driven at distinct frequencies with one greater than the other ( $\Omega \gg \omega$ ).
- To probe an interesting system with a bidirectional diffusive coupling to concur single and multiple VR.

Furthermore, a system of linear coupled anharmonic oscillators is capable of imitating the dynamics of many naturally existing systems, including the dynamics of interacting species in a fluctuating environment to find the probability of the survival of species [34].

The lay-out of the paper is as follows: in §2, a detailed description of the observation of VR and antiresonance in one-way coupled system is presented with numerical and experimental results. Section 3 discusses the detection of multiple VR and antiresonance in a bidirectionally coupled system with the necessary numerical

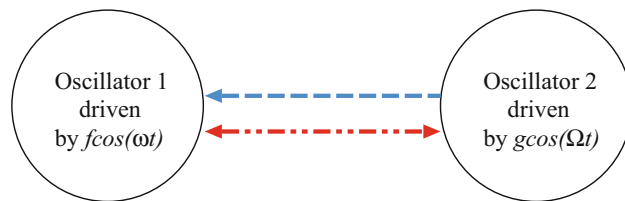


**Figure 1.** Case 1: (Blue line) One-way coupling scheme of the oscillators. Case 2: (Red line) Mutually interacting oscillators. The oscillators are driven by harmonic signals ( $f \cos \omega t$  and  $g \cos \Omega t$ ) of amplitudes  $f$ ,  $g$  and frequencies  $\omega$ ,  $\Omega$ .

and experimental support. Finally, conclusions are given in §4. An effort has been made to derive an empirical analytical expression for response amplitude  $Q$  and critical high-frequency amplitude  $g_{\max}$  for both coupling schemes and are presented in appendices.

## 2. Unidirectionally coupled oscillators

Unidirectionally coupled structures do play a key role in potential applications ranging from the construction of electronic sensors [35] to modelling of repressilators [36]. In the present case, we consider a system of unidirectionally coupled anharmonic oscillators in which the first oscillator is modulated by a high-frequency signal ( $g \cos(\Omega t)$ ) and the other with the low-frequency periodic forcing component ( $f \cos(\omega t)$ ). The dynamical equations of unidirectionally coupled oscillators are

$$\dot{x} = x - x^3 + g \cos(\Omega t), \quad (1)$$

$$\dot{y} = y - y^3 + \gamma x + f \cos(\omega t), \quad (2)$$

where  $\gamma$  is the coupling coefficient that plays a crucial role in response amplitude. To substantiate the presence of VR and antiresonance in the chosen model, we have calculated the response of  $y(t)$  from the sine and cosine components of Fourier amplitude, which are given by

$$B_s(\omega) = \frac{2}{nT} \int_0^{nT} y(t) \sin(\omega t) dt, \quad (3)$$

$$B_c(\omega) = \frac{2}{nT} \int_0^{nT} y(t) \cos(\omega t) dt, \quad (4)$$

where  $n$  is an integer and  $T = 2\pi/\omega$ . The response amplitude is calculated using the relation

$$Q = \frac{\sqrt{B_s^2 + B_c^2}}{f}, \quad (5)$$

whereas the phase shift with respect to the input signal ( $f \cos \omega t$ ) is given by  $\theta(\omega) = \tan^{-1}(B_s(\omega)/B_c(\omega))$ . To analyse the response amplitude in the parametric space

of  $f$  and  $g$ , we fix the parameters as  $\omega = 500$  and  $\Omega = 2000$ . These frequencies were chosen to provide convenient experimental concurrence, and the results follow in the next section. By varying  $f \in [0, 1]$  and  $g \in [0, 20]$ , one can observe multiple resonance peaks as inferred from figure 2a. It is observed that the coupling strength  $\gamma$  has an effective role in influencing the magnitude of  $Q$  but none with the number of resonant peaks. Therefore,  $\gamma$  is fixed as 1.5. Larger response ( $Q_{\max}$ ) can be obtained at  $f = g = 0.02$  that is measured to be 1.8 and the interval of peaks agrees with the period of low-frequency signal. Figure 2b is plotted by varying  $\omega$  in the range [200, 1000] and  $\Omega \in [1400, 2600]$  for fixed values of  $f = g = 0.02$ . The plot displays two prominent peaks with  $Q_{\max}$  measured as 6.98 at  $\omega = 440$  and 940 within the chosen spectrum of  $\Omega$ . The response amplitude is calculated for different  $\omega$  in the range of [100, 500] as a function of  $\gamma \in [0.01, 1.2]$  to study the effect of coupling strength and is shown in figure 2c. The plot depicts multiple VR at regular intervals of  $\omega$ , but the variation in the magnitude of  $Q$  changes abruptly due to nonlinear damping.

The antiresonance frequencies of the system can be spotted by fixing  $\omega = 550$ ,  $\Omega = 2000$ ,  $f = 0.18$  and scanning  $g \in [0, 20]$ . Figures 2d and 2e show the resonance peak at  $\omega = 500$  and antiresonance locus at  $\omega = 550$  for two different coupling strengths  $\gamma = 0.1$  and 1.5, respectively. The mechanism of antiresonance can be ascribed as the vigorous energy transfer from the oscillator driven by high-frequency signal and at particular frequencies, the amplitude of the oscillator driven by low-frequency signal is limited to a minimum. The behaviour of linear increase in magnitude of the response amplitude as a function of  $\gamma$  can be affirmed from figure 2f, due to the absence of to and fro vibrational energy transfer, as limited by unidirectional coupling. The rate of change in  $Q$  is measured by fitting a straight line to the data and quantified as 0.015.

## 2.1 Experimental results

To ascertain the numerical results, an experimental hardware implementation of the chosen system has been realised. The circuit comprises four dual BIFET TL082 JN operational amplifiers, four AD633 JN multipliers (with 10 times scaling factor), two capacitors, eleven linear resistors and two ATEN function generators to generate low- and high-frequency harmonic signals (figure 3). Functionally, two pairs of operational amplifiers ((OA1,OA3) and (OA2,OA4)) act as the adder and the integrator, respectively. The governing dynamical equations due to Kirchhoff's laws are as follows:

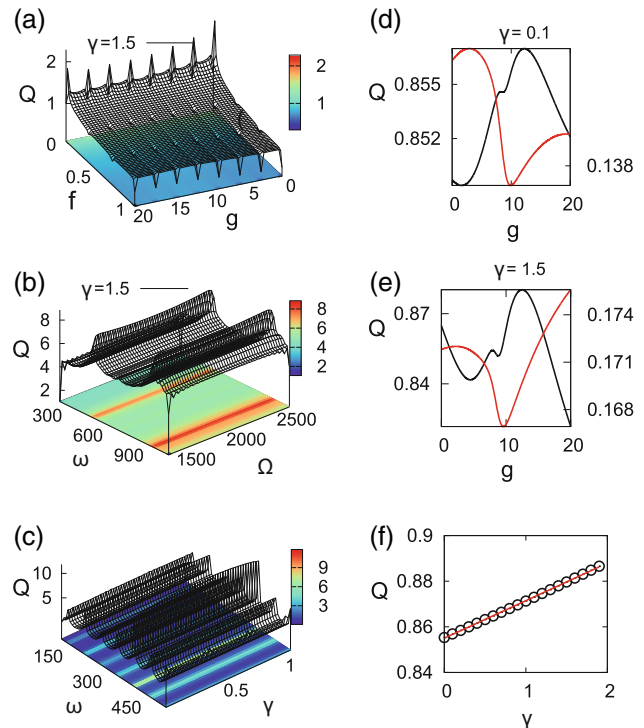


**Figure 2.** (a) The response amplitude  $Q$  in parametric space  $f \in [0, 1]$  and  $g \in [0, 20]$  when  $\omega = 500$ ,  $\Omega = 2000$  and  $\gamma = 1.5$ ; (b)  $Q$  in parametric space  $\omega \in [200, 1000]$ ,  $\Omega \in [1400, 1600]$  when  $f = 0.02$ ,  $g = 0.02$  and  $\gamma = 1.5$ ; (c)  $Q$  as a function of  $\omega \in [100, 500]$  and  $\gamma [0.01, 1.5]$  when  $\Omega = 2000$ ,  $f = g = 0.02$ ; (d)  $Q$  for  $g \in [0, 20]$  with  $f = 0.18$ ,  $\Omega = 2000$  for  $\gamma = 0.1$ , resonance peak (black solid line) at  $\omega = 500$  and antiresonance locus (red solid line) at  $\omega = 550$ ; (e)  $Q$  and antiresonance curve for  $\gamma = 1.5$  and (f) elevation of  $Q$  as a function of  $\gamma$  when  $g = 13.0$ ,  $f = 0.18$ ,  $\omega = 500$  and  $\Omega = 2000$ .

$$C_1 R_4 \frac{dx}{dt} = g \cos(\Omega t) \frac{R_{f1}}{R_2} - x^3 \alpha^2 \frac{R_{f1}}{R_1} + x \frac{R_{f1}}{R_3}, \quad (6)$$

$$C_2 R_9 \frac{dy}{dt} = f \cos(\omega t) \frac{R_{f2}}{R_6} - y^3 \alpha^2 \frac{R_{f2}}{R_5} + y \frac{R_{f2}}{R_8} + x \frac{R_{f2}}{R_7}, \quad (7)$$

where  $\alpha$  is the multiplier constant. To design the circuit with available off-shelf components, the values are fixed as  $R_1 = R_5 = 1 \text{ k}\Omega$ ,  $R_{f1} = R_{f2} = R_2 = R_6 = R_3 = R_8 = R_4 = R_9 = 100 \text{ k}\Omega$ ,  $R_7 = 1 \text{ M}\Omega$  and  $C_1 = C_2 = 10 \text{ }\mu\text{F}$ . The coupling coefficient ( $\gamma$ ) is determined by the ratio  $R_{f2}/R_7$  and is fixed at 0.1 to compare the results with the numerical outcome. Following the procedure illustrated in refs [37,38], the capture of response amplitude has been achieved. The

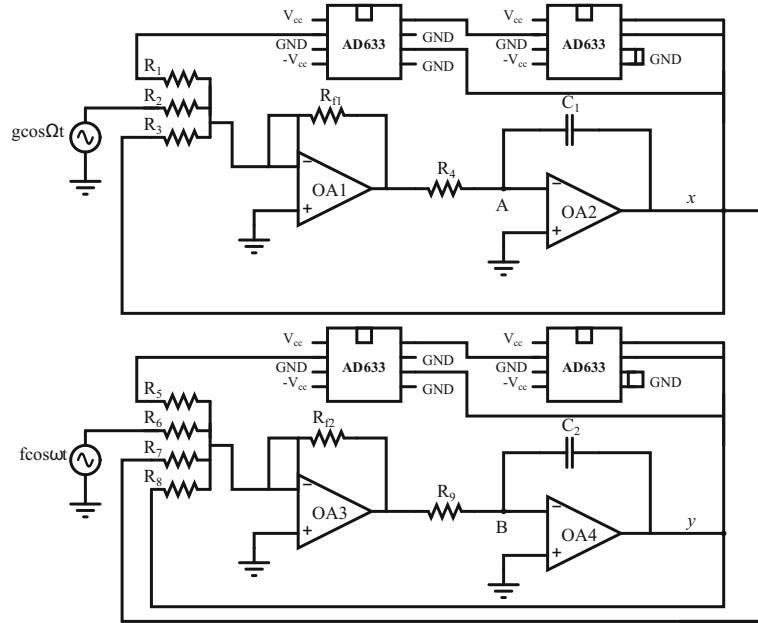


**Figure 3.** Analogue simulation of one-way coupled overdamped oscillators.

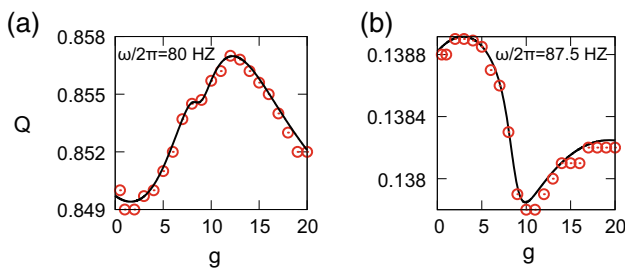


**Figure 4.** Numerical (black solid line) and experimental (red circles) values of  $Q$  for  $g \in [0, 20]$  V with fixed values of  $f = 180$  mV<sub>p</sub>,  $\Omega/2\pi = 318$  Hz: **(a)** VR peak at  $\omega/2\pi = 80$  Hz and **(b)** antiresonance locus at  $\omega/2\pi = 87.5$  Hz.

values of  $\omega/2\pi$ ,  $\Omega/2\pi$  and  $f$  are fixed as 80, 318 Hz and 180 mV<sub>p</sub>, respectively. The response amplitude of the voltage across capacitor  $C_2$  is measured by varying  $g$  from 0 to 20 V<sub>p</sub>, VR is observed and figure 4a compares the numerically and experimentally obtained VR peaks. By fixing the rest of the parameters and altering  $\omega/2\pi = 87.5$  Hz, we observed antiresonance phenomenon. The locus is assessed with numerical prediction and found to be in good agreement as shown in figure 4b.

### 3. Mutually coupled oscillators

Next, we consider a system of mutually coupled overdamped oscillators, each bearing an exclusive monochromatic excitation ( $f \cos(\omega t)$  and  $g \cos(\Omega t)$ ). The

bidirectional coupling scheme enables us to understand much about many natural processes, including neural transmissions [39], interspecies competition, population dynamics of the species [34] and so on. Despite various coupling schemes, bidirectional diffusive coupling is pervasive, and that can facilitate synchronisation and phase coherence, and enhance the detection of weak periodic signals. The occurrence of VR in the chosen model can be assisted by the amplitude of both high-frequency and low-frequency signals at an adjacent node that make it distinct from the classical VR.

Let us consider the following mutually coupled driven system:

$$\dot{x} = x - x^3 + \gamma(x - y) + f \cos(\omega t), \tag{8}$$

$$\dot{y} = y - y^3 + \gamma(y - x) + g \cos(\Omega t). \tag{9}$$

The potential of the system in the absence of external driving is given by

$$U(x, y) = -\frac{x^2}{2} + \frac{x^4}{4} - \frac{y^2}{2} + \frac{y^4}{4} + \gamma \left( xy - \frac{x^2}{2} - \frac{y^2}{2} \right). \tag{10}$$

Depending on the sign of the coefficients of  $x$  and  $y$  and coupling strength  $\gamma$ , the potential can have wells, humps or a combination of both. Here we are interested in potential with four and two wells explicitly relying on  $\gamma$ . For  $\gamma = 0.1$ , eq. (10) unveils symmetric four-well potential with a barrier height of 0.2 in turn equivalent to  $f_c$  as evinced from figure 5a, whereas for  $\gamma = 1.0$



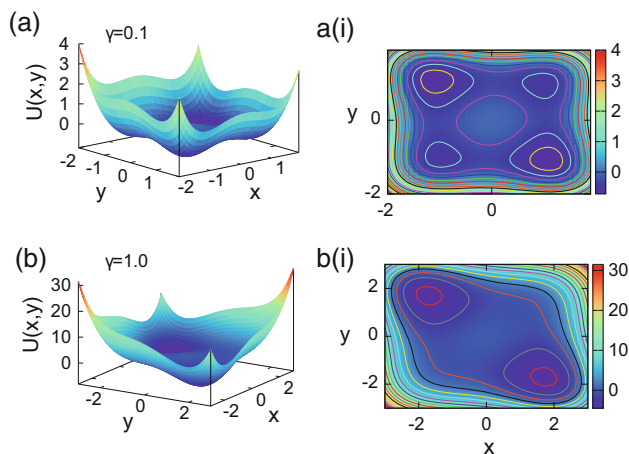


**Figure 5.** (a) Three-dimensional view of symmetric four-well potential for  $\gamma = 0.1$  and (b) transformed two-well potential for  $\gamma = 1.0$ . Parts a(i) and b(i) show the respective contour plots (colour box denotes the height of the potential wells).

the potential shrinks to a double-well potential due to the disappearance of barriers between  $U_{++}$  and  $U_{-+}$  and its symmetric potential ( $U_{--}$  and  $U_{+-}$ ) (figure 5b). One can notice that the barrier height is increased to  $f_c = 1.0$ , when  $\gamma$  is increased. The model has nine equilibrium points, out of which  $(x_1, y_1) = (0, 0)$  and  $(x_{2,3}, y_{2,3}) = (\pm 1, \pm 1)$  for all  $\gamma > 0$ . The stability of  $(x_1, y_1)$  remains unaltered. However, the stability of  $(x_{2,3}, y_{2,3})$  varies from the stable node ( $\gamma < 1.01$ ) to the saddle (from  $\gamma = 1.01$  onwards). The values and the stability of the rest of the equilibrium points rely on the value of  $\gamma$ . For a set of initial conditions  $(x_0, y_0 = \pm 1.0, \pm 1.0)$ , the system settles down to the equilibrium points  $x_{2,3}, y_{2,3}$ , respectively.

Figures 6a and 6b represent the Poincaré surface of section (SOS) of the variable  $x(t)$  sampled at every  $2\pi/\omega$  with respect to the control parameter  $g \in [0, 12]$  corresponding to two different coupling strengths  $\gamma = 0.1$  and  $1.0$ , respectively. The other parameters of the model are kept fixed as  $f = 1.0, \omega = 0.1$  and  $\Omega = 3.0$ . Figure 6a denotes the confinement of the orbit in the potential well  $U_{++}$  for the preferred initial conditions up to the critical threshold vibrational amplitude  $g_c = 7.92$  for  $\gamma = 0.1$ . Beyond  $g_c$ , the oscillation of the orbit gets bounded in  $U_{-+}$ , whereas at the point of a critical threshold the orbits of  $x(t)$  coexist and experience cross well motion that illustrates the well renowned signature of VR. When  $\gamma = 1.0, g_c$  is shifted to a higher value ( $g_c = 9.2$ ) due to the increase in potential barrier height as inferred from figure 6b. As the potential is a two-well potential for  $\gamma = 1.0$ , the dynamics of the system get bounded within  $U_{-+}$  and  $U_{+-}$  wells. The amplitude of the periodic orbit in a single well is

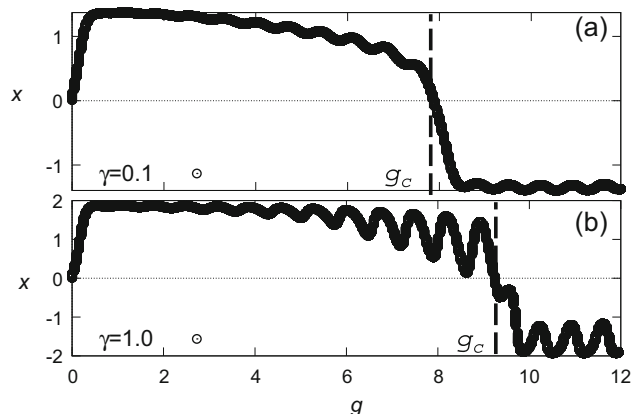


**Figure 6.** Poincaré SOS of  $x(t)$  by setting  $g$  as a control parameter in the range  $g \in [0, 12]$  when  $f = 1.0, \omega = 0.1$  and  $\Omega = 3.0$ : (a) for  $\gamma = 0.1$  and (b) for  $\gamma = 1.0$ .

increased for higher coupling strength ( $\gamma = 1.0$ ) as a consequence of an increase in the depth of the potential wells as seen by comparing figures 5a and 5b. Moreover, period-doubling bifurcation or chaos is exempted in the chosen parametric space, because of the stability of the fixed points in this region. Even though the amplitude of the orbits differs as a function of coupling strength, the time period of oscillation remains constant, equivalent to  $T = 2\pi/\omega$ .

For numerical evaluation of the response amplitude of  $x(t)$  in eq. (8), same set of equations that assesses the Fourier amplitude of the signal is considered (eqs (3)–(5)). To start with, the non-monotonic variation of  $Q$  is assessed by simultaneous scanning of  $f \in [0.01, 0.5]$  and  $g \in [0, 12.0]$  with fixed values of  $\omega = 500, \Omega = 2000$  and  $\gamma = 1.0$ , as shown in figure 7a. This figure shows four resonant peaks and among them the peak at  $g = 4.0$  is found to be with maximum response,  $Q_{\max} = 15.4$ . Moreover, upon close inspection one could visualise the presence of multiple antiresonance loci in the fabric. To track the response of  $x(t)$  in the parametric space of frequencies,  $\omega \in [100, 300]$  and  $\Omega \in [800, 1100], Q$  is computed by fixing  $f = 0.05, g = 0.1, \gamma = 1.0$  and shown in figure 7b. The plot displays consistent alternative peaks and loci at overtones found at  $\omega = 180, 280$ , etc. with average  $Q_{\max} = 0.62$ . When compared with unidirectional coupling (figure 2b), it is found that the interval between harmonic frequencies is reduced and thus one could get more number of resonant peaks due to the mutual transfer of energy. Figure 7c is plotted to analyse the influence of coupling strength on  $Q$  in the range of  $\gamma \in [0.01, 1.5]$  for a spectrum of  $\omega \in [100, 500]$  when  $f = 0.05, g = 0.1$  and  $\Omega = 2000$ . One could infer multiple VR peaks associated with nonlinear variations in  $Q$  from the plot due to the intrinsic nonlinearity present in the

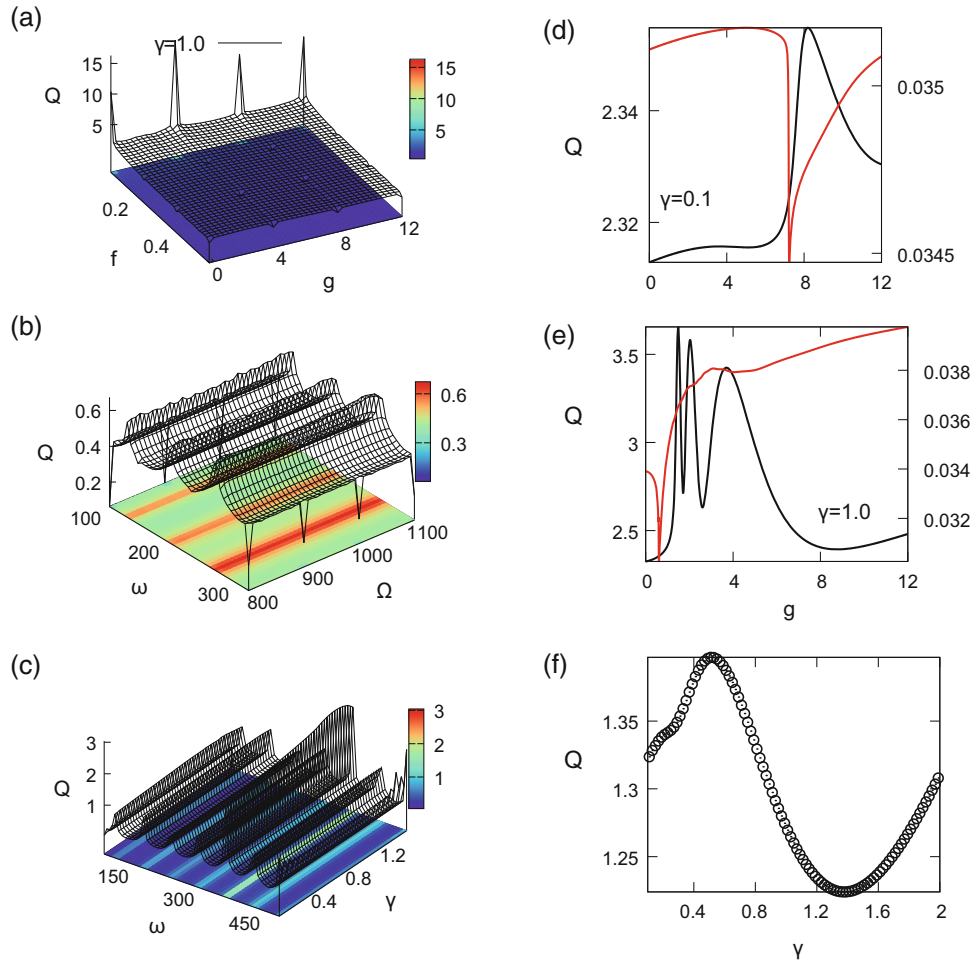


**Figure 7.** (a) The response amplitude  $Q$  by scanning  $f \in [0.01, 0.5]$  and  $g \in [0, 12]$  when  $\omega = 500$ ,  $\Omega = 2000$  and  $\gamma = 1.0$ ; (b)  $Q$  in parametric space  $\omega \in [100, 300]$ ,  $\Omega \in [800, 1100]$  when  $f = 0.05$ ,  $g = 0.1$  and  $\gamma = 1.0$ ; (c)  $Q$  as a function of  $\omega \in [100, 500]$  and  $\gamma [0.01, 1.5]$  when  $\Omega = 2000$ ,  $f = 0.05$  and  $g = 0.1$ ; (d)  $Q$  for  $g \in [0, 12]$  with  $f = 0.05$ ,  $\Omega = 2000$  for  $\gamma = 0.1$ , resonance peak at  $\omega = 500$  and antiresonance locus at  $\omega = 150$ ; (e) same parameters were chosen as if to compute (d) except with  $\gamma = 1.0$ , triple resonant peak is observed for  $\omega = 500$  and a single antiresonant locus for  $\omega = 150$  and (f) plot of  $Q$  as a function of  $\gamma \in [0.1, 2]$  for fixed values of  $g = 8.1$ ,  $f = 0.1$ ,  $\omega = 500$  and  $\Omega = 2000$ .

model. Higher magnitude of  $Q_{\max}$  is observed at one of the harmonic frequencies ( $\omega = 380$ ) that can be affirmed from the figure.

In an attempt to determine the antiresonant frequencies, we have chosen the values of parameters as  $\Omega = 2000$ ,  $f = 0.05$  and  $\gamma = 0.1$ . When  $\omega = 150$ , the model exhibits antiresonance locus as seen from figure 7d. For the same set of parameters, but when  $\omega = 500$ , the model exhibits resonance peak with  $Q_{\max} = 2.35$ . Interestingly, at higher coupling strength  $\gamma = 1.0$ , triple resonant peaks were identified as shown in figure 7e. We found that  $Q_{\max}$  is linearly decreasing with increasing  $g$ . Nevertheless, a single antiresonant locus is detected irrespective of coupling strength as witnessed from the figure. We study the dependence of  $Q_{\max}$  on  $\gamma$  by fixing  $g = 8.1$ ,  $f = 0.1$ ,  $\omega = 500$  and  $\Omega = 2000$ ,

and unlike unidirectional coupling, the plot resembles a cubic polynomial function that is symmetric about the inflection point. This behaviour of the system could be manifested from the cubic nonlinearity present in the model.

To determine the random distribution of time spans ( $\tau_{MR}$ ) spent by the orbit in respective potential wells, we have chosen the parameters of the resonance curves shown in figure 7d. The initial conditions were taken such as the orbit lies in the well  $U_{-+}$  at  $g = g_c$ , to account for the variation in the behaviour of  $\tau_{MR}$ . When  $g = g_c$ ,  $\tau_{MR}$  in  $U_{++}$  is very short and in  $U_{-+}$  it is close to  $2\pi/\omega$  (figure 8a). As  $g \rightarrow g_{\max}$ , the value of  $\tau_{MR}$  in both the wells are found to be equal to the time period of the low-frequency driving, as evident from figure 8b. The logarithmic plot of  $\tau_{MR}$  vs. the factor  $1/(g - g_c)$

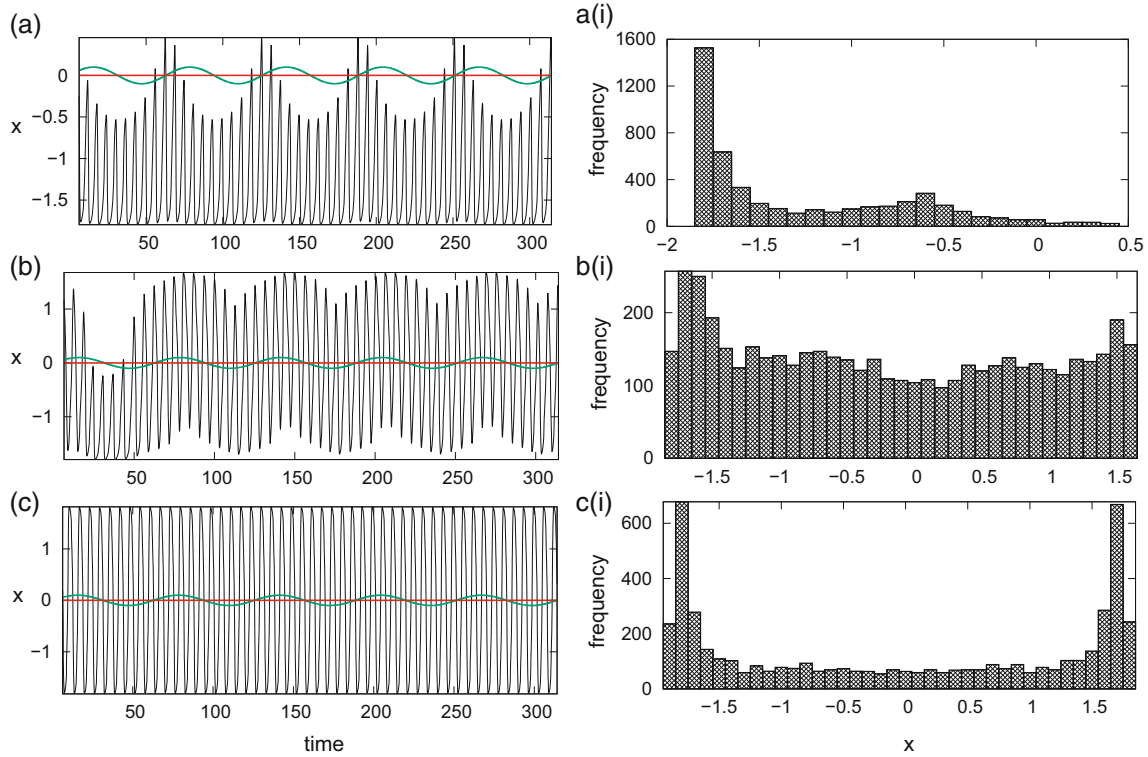


**Figure 8.** Time traces of the trajectory  $x$  for a fixed set of parameters fitting the resonance curve of figure 7d: (a) at  $g = g_c = 7.0$ , (b) at  $g = g_{max} = 8.2$  and (c) at  $g = 12$ . The corresponding subplots depict the distribution of points in respective potential wells.

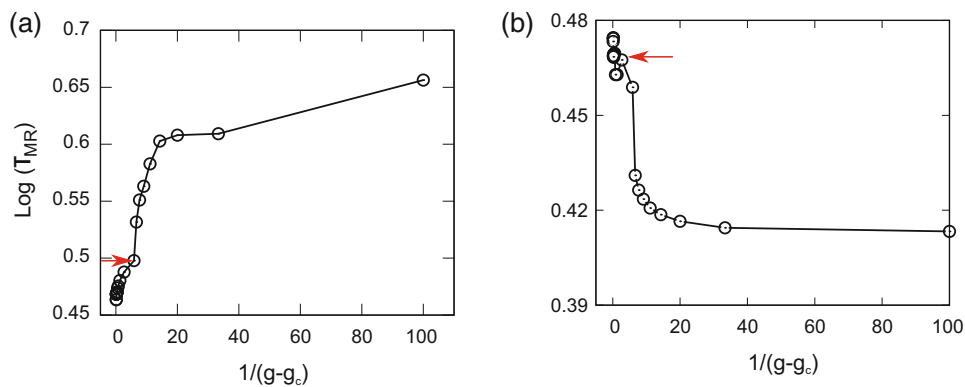


**Figure 9.** Logarithmic mean residence time of the orbit: (a) in the well  $U_{++}$  and (b) in the well  $U_{-+}$  vs.  $1/(g - g_c)$ . The arrow mark in the plot indicates  $\tau_{MR}$  at  $g = g_{max}$ .

confirms the gradual decrement in mean residence times beyond  $g_{max}$  in  $U_{++}$ , whereas in  $U_{-+}$  it decreases as  $g_c \rightarrow g_{max}$  and then increases to the maximum value at  $g = g_{max}$  (figure 9). When  $g$  is increased above  $g_{max}$ , the value of  $\tau_{MR}$  decreases in both the wells. To reassert, we found that as  $g$  increases from  $g_c$ ,  $\tau_{MR}$  in the well  $U_{-+}$  remains close to  $T$ , whereas in  $U_{++}$  it increases to  $T$  until  $g$  reaches  $g_{max}$ . At  $g = g_{max}$ , the time span of the orbit in both the wells is equal to  $T$  and then decreases to  $T/2$  beyond  $g_{max}$ . The time trace and spatial distribution

of the orbit in the active potential wells at  $g = 12$  are shown in figure 8c.

### 3.1 Experimental results

Equivalent analogue simulation of eq. (8) is achieved by employing six dual BIFET TL082 JN operational amplifiers, four AD633 JN multipliers (10 times scaling), two capacitors, 20 linear resistors and two ATEN function generators as shown in figure 10.

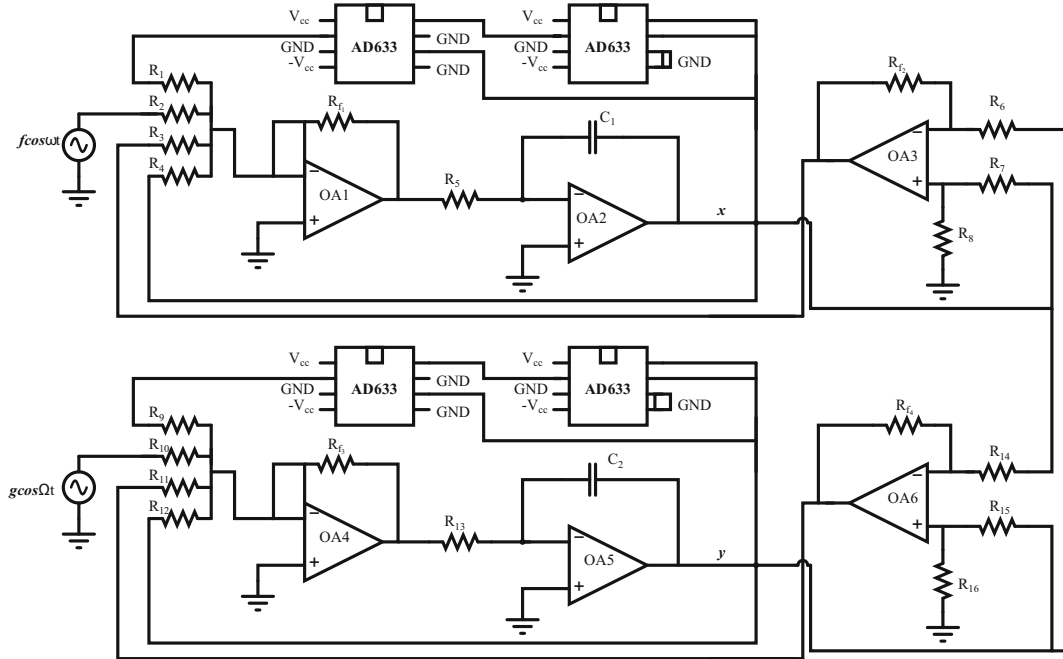


**Figure 10.** Analogue simulation of mutually coupled overdamped oscillator.

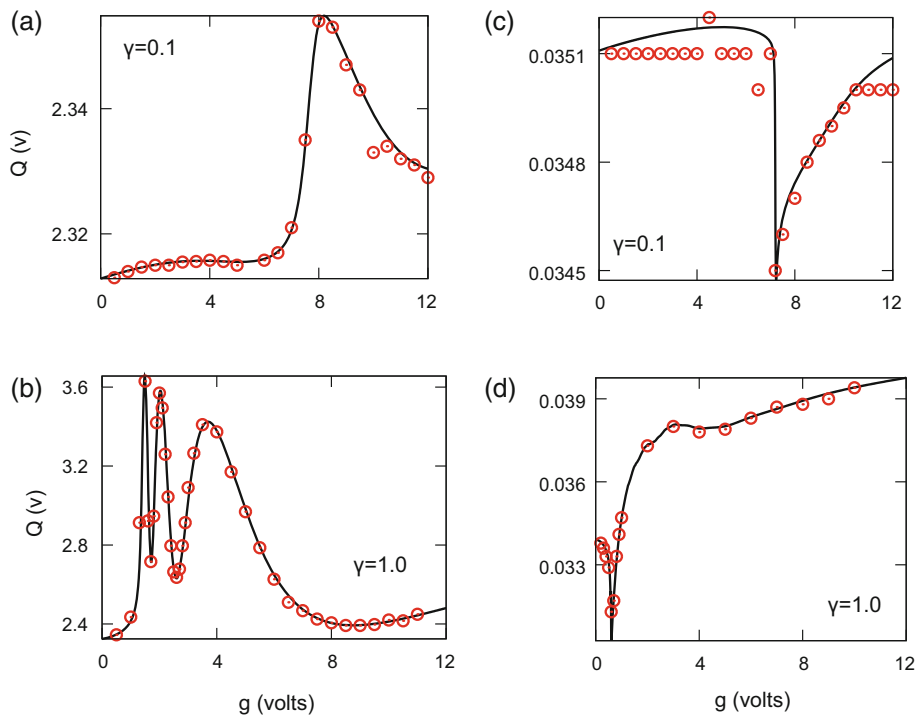


**Figure 11.** Numerical (solid line) and experimental (circles) values of  $Q$  for various values of  $g \in [0, 12]$  V for  $f = 50$  mV<sub>p</sub> and  $\Omega/2\pi = 318$  Hz. **(a)** Single resonance peak for  $\gamma = 0.1$  and  $\omega/2\pi = 80$  Hz, **(b)** triple resonant peaks for  $\gamma = 1.0$  and  $\omega/2\pi = 80$  Hz and **(c, d)** antiresonance locus for  $\omega/2\pi = 24$  Hz with  $\gamma = 0.1$  and  $1.0$ , respectively.

On applying Kirchoff's laws to the circuit, we obtain

$$C_1 R_5 \frac{dx}{dt} = f \cos(\omega t) \frac{R_{f1}}{R_2} - x^3 \alpha^2 \frac{R_{f1}}{R_1} + x \frac{R_{f1}}{R_4} + \frac{R_{f2}}{R_6} (x - y) \frac{R_{f1}}{R_3}, \quad (11)$$

$$C_2 R_{13} \frac{dy}{dt} = g \cos(\omega t) \frac{R_{f3}}{R_{10}} - y^3 \alpha^2 \frac{R_{f3}}{R_9} + y \frac{R_{f3}}{R_{12}} + \frac{R_{f4}}{R_{14}} (y - x) \frac{R_{f3}}{R_{11}}. \quad (12)$$



The values of the resistors and the capacitors are fixed as:  $R_1 = R_9 = R_5 = R_{13} = 10 \text{ k}\Omega$ ,  $R_{f2} = R_{f4} = R_6 = R_{14} = R_8 = R_{16} = 1 \text{ k}\Omega$ ,  $R_{f1} = R_{f3} = R_2 = R_4 = R_{10} = R_{12} = 100 \text{ k}\Omega$ ,  $C_1 = C_2 = 0.01 \text{ }\mu\text{F}$ , and the coupling strength ( $\gamma$ ) between the oscillators is determined by the ratio  $R_{f1}/R_3$  and  $R_{f3}/R_{11}$ . Two unit gain differential amplifiers (OA3 and OA6) were imposed for mutual diffusive coupling. The magnitude spectrum of the voltage drop across capacitor  $C_1$  is evaluated using the AGILENT (DSO-X-2006) oscilloscope spectrum analyser. Initially, the response  $Q$  of the signal is traced as a function of  $g$  for  $\gamma = 0.1$  by keeping the values of  $R_3 = R_{11} = 1 \text{ M}\Omega$ . The control parameters are fixed as  $\omega/2\pi = 80 \text{ Hz}$ ,  $\Omega/2\pi = 318 \text{ Hz}$  and  $f = 50 \text{ mVp}$ . By altering the value of  $g$  from 0.5 to 12  $V_p$ , we obtained resonance peak with  $g_{\max}$  at 8.0  $V_p$ . Figure 11a compares the response of the low-frequency signal with numerically simulated results and the outcomes agree with each other. With the same set of parameters and by reducing  $\omega/2\pi = 24 \text{ Hz}$ , we obtain the antiresonant locus that can be affirmed from figure 11c. Further, we are interested in larger coupling strength, say  $\gamma = 1.0$ , which can be achieved by fixing the values of  $R_3 = R_{11} = 100 \text{ k}\Omega$ . By following the same procedure, we obtained three consecutive VR peaks with enhanced response when compared to  $\gamma = 0.1$ . Figure 11b portrays the perfect match between numerically simulated and experimentally obtained multiple VR peaks. However, a single antiresonant locus can be found experimentally at  $\omega/2\pi = 24 \text{ Hz}$  and figure 11d verifies the correlation of the values between experiment and numerics. Moreover, from experimental heuristics, we found that the accuracy of the experimental outcome enhances when the measure of  $Q$  is pronounced, that is when  $Q$  is measured in a scale of a few volts.

#### 4. Conclusion

Generally, in VR, biharmonic signals are deliberately modulated to evince the resonance phenomenon. On the contrary, here, efforts were made to prove that no superposition of signals is required to achieve non-monotonic variation in the system's response. Rather, interacting oscillators can induce resonance in one of the subsystems in accordance with the high-frequency amplitude variation. To establish the observation, we had chosen two coupled anharmonic oscillators, each of which is driven by distinct frequencies employing unidirectional and bidirectional coupling. We had detected the non-monotonic variation in the system's response driven by a low-frequency signal in both cases, classically

termed as VR. This sort of behaviour is the manifestation of non-monotonic dependence of the model's effective stiffness on the amplitude of high-frequency forcing. Interestingly, we found multiple VRs and antiresonance loci for the given choice of parameters in both coupling schemes due to the multistability of the chosen model. The response of the low-frequency component is found to be influenced by the high-frequency amplitude in a resonant way at harmonic frequencies. We had effectively probed the influence of coupling strength on the resonant interaction of coupled oscillators, and it is found that stronger coupling will lead to higher response amplitude. Even though unidirectional coupling may induce larger responses, the mutual diffusive coupling increases the probability of occurrence of resonance in the model. In other words, bidirectional diffusive coupling enhanced the interaction between the coupled oscillators ensuring more spans of entrainment domains. Moreover, it has been detected that the intrawell motion between the potential wells is assimilated as the mechanism of VR in mutual coupling. Upon calculating the mean residence time spent by an orbit in active potential wells, we found that at  $g = g_{\max}$ , the value of  $\tau_{\text{MR}}$  is equal to integer multiples of the time period of the low-frequency driving ( $T$ ) in mutually coupled oscillators. Antiresonance locus as a counterpart of resonance peaks can be used to identify the symmetry of the coupled oscillators and the spot of perturbations in the system. Critically, antiresonance is induced in the model as a consequence of the excessive vibrational energy transfer to an adjacent oscillator which reduces the amplitude to a minimum value at particular frequencies. The experimental substantiation of the remarked phenomenon has also been accomplished by means of analogue simulations and the results are in good agreement with numerical computations. Since interacting dynamical systems are ubiquitous in nature, we believe that the results of the present investigation can find significant applications in communication technologies, neuronal dynamics and mechanical engineering.

#### Acknowledgement

A Jeevarekha thanks the Department of Science and Technology for the support provided in the form of DST INSPIRE Fellowship.

#### Appendix A. Unidirectionally coupled oscillators—Theoretical approach

We have made an attempt to provide an empirical solution to the considered models. While solving eq. (1), the

solution for  $\dot{x}$  is determined to be

$$x = \frac{g \cos(\Omega t - \theta_1)}{\sqrt{1 + \Omega^2}}, \tag{A1}$$

where  $\theta_1 = \tan^{-1}(\Omega)$ . Upon substituting the value of  $x$ , the standard method of variable decomposition  $y(t) = Y(t, \omega t) + \psi(t, \Omega t)$  is applied to eq. (2), where  $Y(t, \omega t)$  and  $\psi(t, \Omega t)$  correspond to slow and fast moving components of the response, respectively [40]. Employing the decomposition method and averaging the fast moving components, one gets

$$\dot{Y} = Y(1 - 3\bar{\psi}^2) - Y^3 + f \cos(\omega t), \tag{A2}$$

$$\dot{\psi} = g_1 \cos(\Omega t) \tag{A3}$$

with  $g_1 = \gamma g / (\sqrt{1 + \Omega^2})$ . Considering the value of  $\bar{\psi}^2$  from eqs (A3), (A2) becomes

$$\dot{Y} - Yc_1 + Y^3 = f \cos(\omega t), \tag{A4}$$

where  $c_1 = 1 - (3g_1^2/2\Omega^2)$  and it is quite evident from the above equation that the shape of the potential depends on the value of  $g$ ,  $\gamma$  and  $\Omega$ . When  $c_1 > 0$ , a double-well potential is obtained with its maxima and minima located at  $Y_1^* = 0$  and  $Y_{2,3}^* = \pm\sqrt{c_1}$ , respectively. On the other hand, when  $c_1 < 0$ , the shape of the potential becomes a single well with its minima located at  $Y_1^* = 0$ . Also, from eq. (A4), it is evident that the effective parameters of the system get affected due to resonance.

The critical value of  $g$  at which the resonance is observed can be deduced from the following relation:

$$g_{\max} = \sqrt{\frac{2\Omega^2(\Omega^2 + 1)}{3\gamma^2}}. \tag{A5}$$

As the oscillators are one-way coupled,  $f$  and  $\omega$  do not affect  $g_{\max}$ . As previously mentioned, if  $g < \sqrt{(2\Omega^2(\Omega^2 + 1))/3\gamma^2}$ , there exist two minima in  $\pm\sqrt{c_1}$  and the deviation from the minima  $Y_{2,3}^*$  can be calculated by substituting  $Z = Y - Y_{2,3}$  in eq. (A4). Upon substitution of  $z$  and using the linearisation, one gets a modified equation as

$$\dot{z} = s_1 z + f \cos \omega t, \tag{A6}$$

where  $s_1 = 2c_1$ . From the above equation, the response amplitude and the phase shift are analytically calculated to be

$$Q = \frac{1}{\sqrt{\omega^2 + 4c_1^2}}, \tag{A7}$$

$$\theta_2 = \tan^{-1} \frac{\omega}{s_1}. \tag{A8}$$

Else when  $g > \sqrt{(2\Omega^2(\Omega^2 + 1))/3\gamma^2}$ , there exists only one minimum at  $Y_1^*$  and the response amplitude

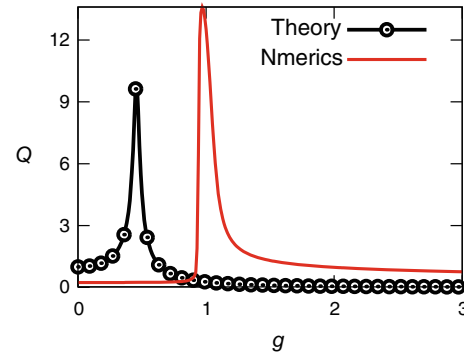


**Figure 12.** Comparison of numerical and analytical values of  $Q$  for fixed values of  $f = 0.05$ ,  $\omega = 0.1$  and  $\Omega = 0.5$  when the coupling strength  $\gamma = 1.0$ .

and phase shift now become

$$Q = \frac{1}{\sqrt{\omega^2 + c_1^2}}, \tag{A9}$$

$$\theta_2 = \tan^{-1} \frac{\omega}{c_1}. \tag{A10}$$

The response amplitude is calculated using eq. (A9) when  $\omega = 0.1$ ,  $\Omega = 0.5$ ,  $f = 0.05$  and the outcomes are compared in figure 12.

### Appendix B. Mutually coupled oscillators—Theoretical approach

Further, as the process of obtaining analytical solution for mutually coupled oscillators is tedious, a highly approximated method of solution is proposed here. It starts with the addition of eqs (8) and (9) as

$$\dot{x} + \dot{y} = (x + y) - (x^3 + y^3) + f \cos \omega t + g \cos \Omega t. \tag{B1}$$

Replacing  $x = X(t, \omega t) + \psi(t, \Omega t)$  and  $y = Y(t, \omega t) + \psi(t, \Omega t)$  and on resolving slow and fast components, we obtain

$$\dot{X} + \dot{Y} = (X + Y)[1 - 3\bar{\psi}^2] - (X^3 + Y^3) + f \cos \omega t, \tag{B2}$$

$$\dot{\psi} = \frac{g \cos \Omega t}{2}. \tag{B3}$$

After substituting the value of  $\psi$  using eq. (B3) and by considering  $X + Y = A$ , the linearised form of equation will be obtained as  $\dot{A} = c_1 A + f \cos \omega t$ . Then the solution  $A$  is determined to be

$$A = \frac{f \cos(\omega t - \phi)}{\sqrt{c_1^2 + \omega^2}}, \tag{B4}$$

where  $c_1 = [(3g^2/4\Omega^2) - 1]$  and  $\phi = \tan^{-1}(\omega/c_1)$ .

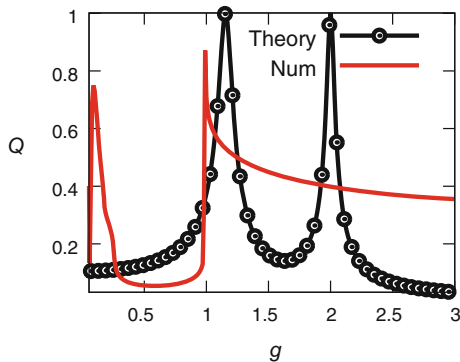


**Figure 13.** Variation of  $Q$  with  $g$  for  $\omega = 0.1$ ,  $\Omega = 1.0$ ,  $\gamma = 1.0$  and  $f = 0.001$ . Theoretical output has been appropriately scaled down for better fit.

Similarly, on subtracting eqs (8) and (9), we get

$$\dot{x} - \dot{y} = (x - y) - (x^3 - y^3) + 2\gamma(x - y) + f \cos \omega t - g \cos \Omega t. \tag{B5}$$

Again by replacing  $x = X + \psi$  and  $y = Y - \psi$  and on resolving slow and fast components, we obtain

$$\dot{X} - \dot{Y} = (X - Y)[1 - 3\bar{\psi}^2 + 2\gamma] - (X^3 - Y^3) + f \cos \omega t, \tag{B6}$$

$$\dot{\psi} = -\frac{g \cos \Omega t}{2}. \tag{B7}$$

After substituting the value of  $\psi$  using eq. (B7) and by having  $X - Y = B$ , the solution becomes

$$B = \frac{f \cos(\omega t - \phi_1)}{\sqrt{c_2^2 + \omega^2}}, \tag{B8}$$

where  $c_2 = (3g^2/4\Omega^2) - 1 - 2\gamma$  and  $\phi_1 = \tan^{-1}(\omega/c_2)$ . On solving  $A$  and  $B$ , the response amplitude of the coupled system is found to be

$$Q = \frac{\kappa \cos(\omega t - \theta)}{2}, \tag{B9}$$

where

$$\kappa = \sqrt{\alpha^2 + \beta^2 + 2\alpha\beta \cos(\phi - \phi_1)},$$

$$\theta = \tan^{-1} \frac{\alpha \sin \phi + \beta \sin \phi_1}{\alpha \cos \phi + \beta \cos \phi_1}.$$

The values of  $\alpha$  and  $\beta$  are  $1/(\sqrt{c_1^2 + \omega^2})$  and  $1/(\sqrt{c_2^2 + \omega^2})$ , respectively. The fitness of the theoretical model to numerical outcomes is shown in figure 13.

## References

- [1] L Gammaitoni, P Hänggi, P Jung and F Marchesoni, *Rev. Mod. Phys.* **70**, 223 (1998)
- [2] A Kenfack and K P Singh, *Phys. Rev. E* **82**, 046224 (2010)
- [3] I Blekhman and V S Sorokin, *Nonlinear Dyn.* **1** (2018)
- [4] R Benzi, A Sutera and A Vulpiani, *J. Phys. A* **14**, L453 (1981)
- [5] I Y Lee, X L Liu, B Kosko and C W Zhou, *Nano Lett.* **3**, 1683 (2003)
- [6] J J Collins, T T Imhoff and P Grigg, *J. Neurophysiol.* **76**, 642 (1996)
- [7] J K Douglass, L Wilkens, E Pantazelou and F Moss, *Nature (London)* **365**, 337 (1993)
- [8] J E Levin and J P Miller, *Nature (London)* **380**, 165 (1996)
- [9] P S Landa and P V E McClintock, *J. Phys. A* **33**, L433 (2000)
- [10] A Zaikin, J García-Ojalvo, L Schimansky-Geier and J Kurths, *Phys. Rev. Lett.* **88**, 010601 (2001)
- [11] E Ullner, A Zaikin, J García-Ojalvo, R Bäscones and J Kurths, *Phys. Lett. A* **312**, 348 (2003)
- [12] A Daza, A Wagemakers, S Rajasekar and M A F Sanjuán, *Commun. Nonlinear Sci. Numer. Simul.* **18**, 411 (2013)
- [13] J H Yang and B Liu, *Chaos* **20**, 033124 (2010)
- [14] S Rajasekar, J Used, A Wagemakers and M A F Sanjuán, *Commun. Nonlinear Sci. Numer. Simul.* **17**, 3435 (2012)
- [15] A Jeevarekha and P Philominathan, *Pramana – J. Phys.* **86(5)**, 1031 (2016)
- [16] S Ghosh and D S Ray, *Phys. Rev. E* **88**, 042904 (2013)
- [17] L M Pecora and T L Carroll, *Phys. Rev. Lett.* **64**, 821 (1990)
- [18] A Prasad, M Dhamala, B M Adhikari and R Ramaswamy, *Phys. Rev. E* **81**, 027201 (2010)
- [19] M Daniel, R Mirollo, H Strogatz and A Wiley, *Phys. Rev. Lett.* **101**, 129902 (2008)
- [20] Y Wang, D T Chik and Z D Wang, *Phys. Rev. E* **61(1)**, 740 (2000)
- [21] A Lovera, B Gallinet, P Nordlander and O J Martin, *ACS Nano* **7(5)**, 4527 (2013)
- [22] B Deng, J Wang and X Wei, *Chaos* **19(1)**, 013117 (2009)
- [23] C Yao and M Zhan, *Phys. Rev. E* **81**, 061129 (2010)
- [24] V M Gandhimathi, S Rajasekar and J Kurths, *Phys. Lett. A* **360**, 279 (2006)
- [25] V M Gandhimathi and S Rajasekar, *Phys. Scr.* **76(6)**, 693 (2007)
- [26] A Jeevarekha, M Santhiah and P Philominathan, *Pramana – J. Phys.* **83(4)**, 493 (2014)
- [27] R Jothimurugan, K Thamilmaran, S Rajasekar and M A F Sanjuán, *Nonlinear Dyn.* **83(4)**, 1803 (2016)
- [28] S Jeyakumari, V Chinnathambi, S Rajasekar and M A F Sanjuan, *Phys. Rev. E* **80(4)**, 046608 (2009)
- [29] X X Wu, C Yao and J Shuai, *Sci. Rep.* **5**, 7684 (2015)
- [30] Z Agur, *Comput. Math. Methods Med.* **1(3)**, 237 (1998)
- [31] W Dámbrógio and A Fregolent, *J. Sound Vib.* **236(2)**, 227 (2000)

- [32] B Lysyansky, O V Popovych and P A Tass, *J. Neural Eng.* **8**(3), 036019 (2011)
- [33] H Zhang, H Chang and W Yuan, *Microsyst. Nanoeng.* **3**, 17023 (2017)
- [34] G Baxter, J McKane and B Tarlie, *Phys. Rev. E* **71**, 011106 (2005)
- [35] B Razavi, *Fundamentals of microelectronics* (Wiley, New York, 2008)
- [36] M B Elowitz and S Leibler, *Nature* **403**, 335 (2000)
- [37] J P Baltanás, L López, I I Blechman, P S Landa, A Zaikin, J Kurths and M A F Sanjuán, *Phys. Rev. E* **67**, 066119 (2003)
- [38] R Jothimurugan, K Thamilaran, S Rajasekar and M A F Sanjuán, *Int. J. Bifurc. Chaos* **23**, 1350189 (2013)
- [39] K L Babcock and R M Westervelt, *Physica D* **28**, 305 (1987)
- [40] F Ci-Jun and L Xian-Bin, *Chin. Phys. Lett.* **29**, 050504 (2012)